Heisenberg scaling of imaging resolution by coherent enhancement

Robert McConnell, Guang Hao Low, Theodore J. Yoder, Colin D. Bruzewicz, Isaac L. Chuang, John Chiaverini, and Jeremy M. Sage

Heisenberg scaling of imaging resolution by coherent enhancement

Robert McConnell,[1, *] Guang Hao Low,[2] Theodore J. Yoder,[2] Colin D. Bruzewicz,[1] Isaac L. Chuang,[2] John Chiaverini,[1] and Jeremy M. Sage[1]

[1]*Lincoln Laboratory, Massachusetts Institute of Technology, Lexington, Massachusetts 02420, USA*
[2]*Massachusetts Institute of Technology, Cambridge, Massachusetts 02139, USA*
(Dated: August 28, 2017)

Classical imaging works by scattering photons from an object to be imaged, and achieves resolution scaling as $1/\sqrt{t}$, with t the imaging time. By contrast, the laws of quantum mechanics allow one to utilize quantum coherence to obtain imaging resolution that can scale as quickly as $1/t$ – the so-called "Heisenberg limit". However, ambiguities in the obtained signal often preclude taking full advantage of this quantum enhancement, while imaging techniques designed to be unambiguous often lose this optimal Heisenberg scaling. Here, we demonstrate an imaging technique which combines unambiguous detection of the target with Heisenberg scaling of the resolution. We also demonstrate a binary search algorithm which can efficiently locate a coherent target using the technique, resolving a target trapped ion to within 0.3% of the $1/e^2$ diameter of the excitation beam.

I. INTRODUCTION

Imaging is an essential task in many areas of science, from biology to astronomy to condensed matter physics. Classically, imaging is performed by illuminating a target and collecting those photons which scatter from it. The scale of imaging resolution in this case is set by the wavelength λ of the imaging light and the numerical aperture of the imaging system, but the resolution improves only as the square root of the number of scattered photons and hence as the square root of imaging time t. Especially in situations when the numerical aperture of the imaging system is limited, the practically-achievable resolution can be insufficient to resolve details of interest.

Numerous imaging techniques which outperform the traditional diffraction limit have been demonstrated [1–4]. These techniques typically work by "excluding" targets not within a sub-diffraction-limited area by storing such targets in a non-scattering, "dark" state $|d\rangle$, then scattering imaging photons off of remaining targets in a bright state $|g\rangle$ on a strong transition $|g\rangle \rightarrow |e\rangle$. While these techniques have realized resolution as low as $\lambda/10$ in some cases [5, 6], they are still limited to a classical time scaling of $1/\sqrt{t}$ because they do not utilize the full quantum mechanical coherence of their targets.

By contrast, the coherent properties of a quantum mechanical two-level system in principle allow resolution scaling at the so-called Heisenberg limit, as $1/t$ [7, 8]. A single spin precessing under a Hamiltonian H accumulates phase $\phi = (H/\hbar)t$ and a single measurement of this phase achieves resolution $\Delta\phi = \pi/2$ [9]. If the particle position x can be linearly mapped to H, positional uncertainty $\Delta x \sim \Delta\phi/t$ scaling as $1/t$ can be achieved.

One way to map particle position x to H is to utilize the spatially-varying intensity of a Gaussian beam coupling $|g\rangle$ to $|e\rangle$ and drive a single long pulse. In this case, it is total rotation angle on the Bloch sphere, θ, which
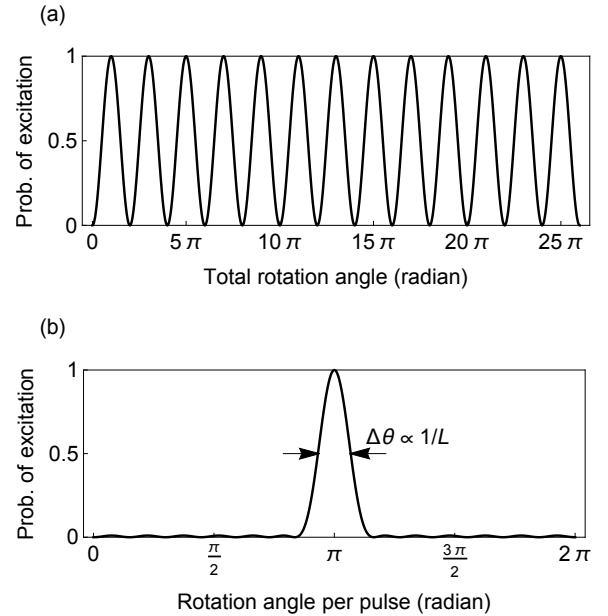
* robert.mcconnell@ll.mit.edu

FIG. 1. (a) Coherent oscillations in a driven two level system produce very narrow features which in principle can be used to achieve Heisenberg-limited resolution, but signal ambiguities often preclude achieving such resolution in practice. (b) A sequence of L pulses of the same overall duration as the drive in (a) can produce an unambiguous single excitation peak whose width nevertheless preserves optimal Heisenberg scaling as $1/L$, by varying the phases ϕ_i of each pulse. Here, $L = 13$.

carries information about the particle position. However, when a single long pulse is used (Figure 1(a)), other rotation angles separated by a multiple of 2π from the correct θ can lead to identical observables, which can render a precise estimation of the actual phase impossible. Techniques to produce unambiguous phase mappings [10–12] often do so at the expense of Heisenberg scaling, returning to a classical scaling $\sim 1/\sqrt{t}$.

In this proof-of-principle experiment, we demonstrate

an imaging technique which exploits quantum mechanical coherence and optimal quantum control to unambiguously resolve a trapped atomic ion with Heisenberg scaling of the resolution. Optimally designed pulse sequences [13] transfer the target ion from its ground state $|g\rangle$ to excited state $|e\rangle$ with a position uncertainty scaling as $1/L$, with L the length of the pulse sequence (Figure 1(b)). By using a binary search algorithm which starts with broad excitation and progressively narrows, we efficiently determine the ion position to within 0.3% of the control beam diameter, with search failure exponentially suppressed in the number of sequence repetitions. To our knowledge, this represents the first experiment to approach Heisenberg-limited scaling in an imaging task. The technique is related to methods that have achieved magnetic field resolution improving as $t^{-0.85}$ [14, 15] and have improved the frequency stability of local oscillators [16]. High-resolution magnetic resonance imaging of a single diamond-NV center within an external magnetic gradient has been achieved via a Fourier-transform technique [17]. In contrast to those phase-estimation techniques, the method we employ here directly obtains positional information via the spatial gradient of the coherent drive's intensity. As a result, we do not require external fields for imaging (other than the coherent control drive) and we achieve rapid imaging of a coherent target in real time, with minimal post-processing of data. This allows achievement of a given resolution much faster than is possible classically, useful in any situation where the available time for imaging is limited. The narrow excitation window as a function of control drive intensity also allows this technique to be used for site-selective addressing of one ion or other coherent target within an array [18–20], and allows straightforward generalization to imaging of multiple targets.

Our quantum-enhanced imaging technique requires a coherent drive coupling the target states $|g\rangle, |e\rangle$ with a Rabi frequency Ω and able to implement arbitrary rotations on the Bloch sphere of an angle $\theta = \Omega t$. Quantum-enhanced imaging is implemented by a sequence of L such rotations. Within such a sequence, each pulse is performed for the same time t_0 and with the same laser intensity such that the rotation angle θ per pulse is the same. However, the phase ϕ_i of each pulse i in the sequence is optimized such that the ion is only transferred from $|g\rangle$ to $|e\rangle$ if the rotation per pulse satisfies $\theta = \pi$ to within an error $\Delta\theta \sim 1/L$ (Figure 1(b)). We here consider a 1-D case, but this technique can readily be generalized to higher dimensions.

The Heisenberg-limited scaling of the error in rotation angle θ can be mapped to position resolution by using the spatially-varying intensity of a Gaussian beam. In particular, for a beam centered at the origin, the ion Rabi frequency as a function of position x obeys

$$\Omega(x) = \Omega_0 e^{-x^2/w^2}, \qquad (1)$$

where w is the beam waist ($1/e^2$ intensity radius) and Ω_0 the ion Rabi frequency at the center of the beam. The po-
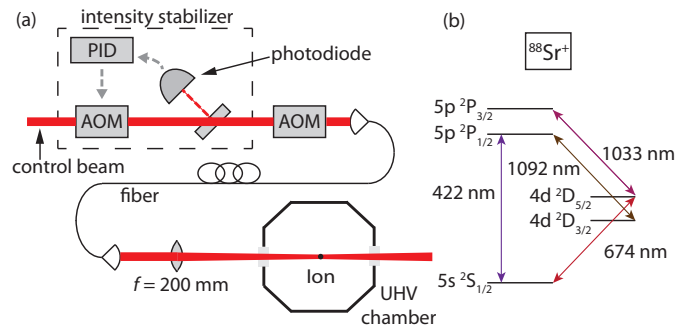

FIG. 2. (a) Schematic of the apparatus used to perform quantum-enhanced imaging. The 674 nm control beam passes through an intensity stabilization circuit (described in text) and then an AOM used to control its intensity. The beam passes through a fiber and then enters the apparatus, where it is focused onto the ion. PID = proportional-integral-differential feedback controller. (b) Relevant level structure in ^{88}Sr$^+$.

sitional mapping is optimized if the excitation occurs at the location of maximum field slope of the beam, that is, if $\Omega(x)t_0 = \pi$ for the point where $|d\Omega/dx|$ is maximized. This maximum occurs when the beam intensity and pulse length t_0 are chosen such that $\Omega_0 t_0 = \pi\sqrt{e}$. For this Ω_0, and at the location of maximum slope $x = w/\sqrt{2}$, the positional error Δx obeys

$$\Delta x = \frac{\Delta\theta \cdot w}{\pi\sqrt{2}}. \qquad (2)$$

By correctly choosing the pulse duration as a function of Rabi frequency, this optimal positional resolution can be retained even as the control beam is scanned to search for the ion location.

The phases that produce such a narrowband excitation are described in [13, 21] and are derived from Chebyshev polynomials. In essence, these pulse sequences trade small probabilities of excitation ("ripples") in the stopband for an optimally narrow passband, in analogy to Chebyshev filters (c.f. Figure 1(b)).

II. APPARATUS

Figure 2 shows the apparatus we use to perform quantum-enhanced imaging. A trapped ^{88}Sr$^+$ ion is confined 50 μm above the surface of a niobium surface electrode trap and is laser-cooled to its motional ground state [22]. The ion is coherently driven on the 674 nm, $|g\rangle = |5S_{1/2}, m = -1/2\rangle \rightarrow |e\rangle = |4D_{5/2}, m = -5/2\rangle$ quadrupole transition with lifetime ~ 0.5 s. Approximately 3 mW of power from a diode laser provide a Rabi frequency of typically $\Omega_0 = 2\pi \times 100$ kHz. This beam is stabilized by transmission through a narrow-linewidth ultra-low-expansion (ULE) glass cavity [23], with the transmitted beam seeding an injection-locked laser which is then amplified by a tapered amplifier. This method

filters out spectral noise ("servo bumps") in the laser which would otherwise cause degradation of the technique. An intensity stabilization circuit is used to limit intensity fluctuations of the control laser at the ion location. A photodiode samples a portion of the beam power; this photodiode signal is sent to a proportional-integral-differential feedback controller which adjusts the modulation input of an acousto-optical modulator (AOM) to maintain constant power. After the intensity stabilizer, we use a second AOM to control the power and phase of the control beam at the ion location. Finally, this output passes through a single-mode fiber and emerges from a fiber launch near the experiment which minimizes angular jitter of the beam. This output is focused on the ion by a lens of focal length 200 mm. By adjusting the lens position with a manual micrometer and measuring the change in ion Rabi frequency with position, we determine the control laser beam waist to be $140 \pm 10\,\mu m$ at the ion location. These measurements also confirm the Gaussian shape of the control beam.

High-fidelity readout of the ion's internal state is accomplished by scattering light from a 422 nm laser which couples $|g\rangle$ but not $|e\rangle$ to the short-lived excited state $5P_{1/2}$; a high-NA lens and external PMT collect scattered photons and allow readout fidelity of 99.99% in 1 ms. Additional repumping lasers at 1092 nm and 1033 nm used at various times during the control and readout sequence prevent population trapping in undesired internal states of the ion.

III. RESULTS

Figure 3 shows the results of applying excitation pulse sequences of varying length to the trapped ion. With the ion initially in $|g\rangle$, a pulse sequence of length L and per-pulse rotation angle θ is applied; afterwards, we measure the final state of the ion. We perform 200 repetitions per point in order to estimate the probability of the transition $|g\rangle \rightarrow |e\rangle$ for each L and θ. For the experiments shown in Figure 3, the ion is located at the center of the beam and the beam intensity adjusted via the control AOM. Figure 3(a) shows a single pulse applied to the ion, in which case a broad excitation $|g\rangle \rightarrow |e\rangle$ occurs which does not well localize the ion. As the number of pulses is increased (Figure 3(b)-(d)), a narrow and unambiguous excitation is achieved. The dashed curves in the figure show the theoretical transfer probability; we demonstrate excitation widths that are in very good agreement with the theoretical predictions.

Figure 4 shows the scaling of the fitted full width half maximum (FWHM) of the peaks in the experimental data as a function of sequence length L. The green curve shows the theoretical prediction with asymptotic L^{-1} scaling, while the classical $L^{-0.5}$ scaling is shown by the black dash-dotted curve. Up to $L = 199$ we observe widths in very good agreement with the theory curve, while for $L > 199$ the width becomes lim-
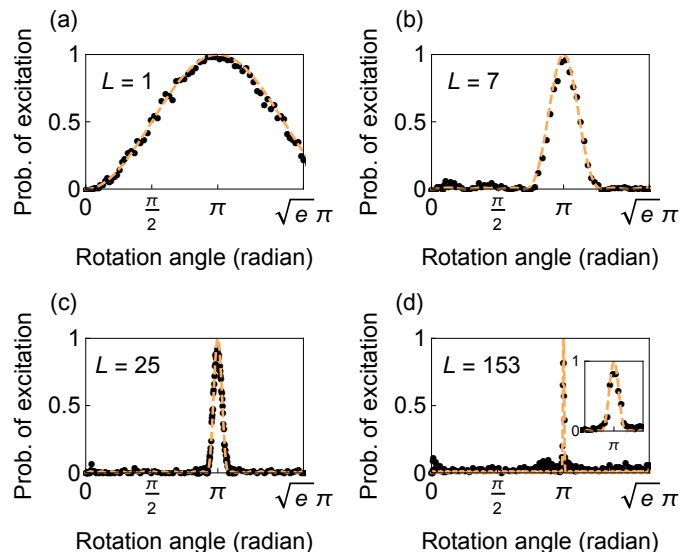

FIG. 3. Examples of quantum-enhanced imaging for (a) a single pulse, (b) a 7-pulse sequence, (c) a 25-pulse sequence, (d) a 153-pulse sequence. The orange dashed curves show model-free theory predictions for the excitation as a function of drive strength. The inset in subplot (d) shows the excitation width and agreement with the model near $\theta = \pi$ for the narrow $L = 153$ sequence; the inset x-axis spans 0.2 radian.
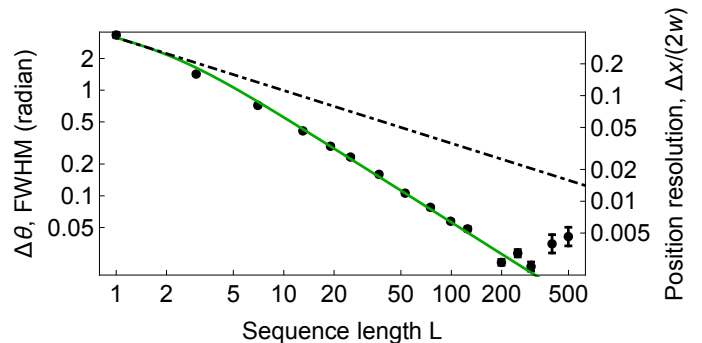

FIG. 4. Scaling of the FWHM of the excitation region as a function of pulse sequence length L. The solid green curve shows the theoretical width that should be achieved (asymptotically scaling as $1/L$),while the black dot-dashed curve shows classical scaling as $L^{-0.5}$.

ited by the finite system coherence time. We note that with per-pulse times of $10\,\mu s$, we are able to perform pulse sequences somewhat longer than the nominal system coherence time of ~ 0.5 ms given by Ramsey measurements, due to partial spin-echo effects during the pulse sequences.

Finally, we demonstrate a binary search technique to locate an ion of an initially unknown location (Figure 5). The essence of the binary search is as follows. An ion of initially unknown location is addressed by the coherent control beam. For convenience we assume the ion is in the half-space $x > 0$ for which the ion Rabi frequency
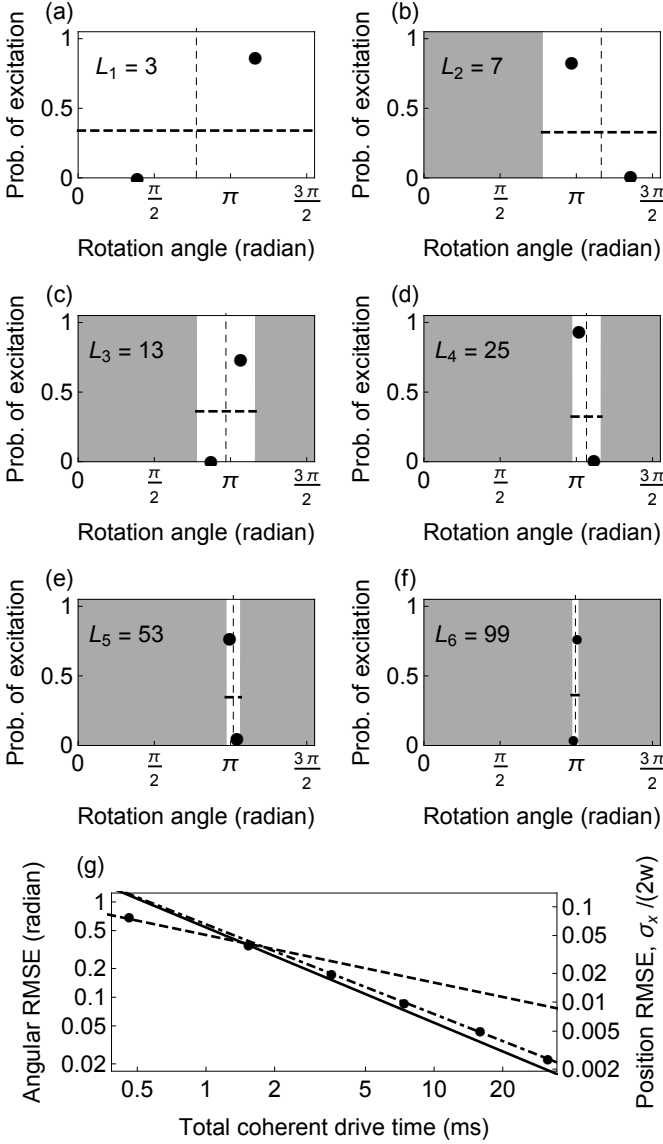
FIG. 5. Demonstration of the logarithmic search technique. The beam is positioned so that its maximum intensity slope is located at the ion position. (a) - (f) Successive pulse sequences of length $L_1 = 3$, $L_2 = 7$, $L_3 = 13$, $L_4 = 25$, $L_5 = 53$, $L_6 = 99$ pulses are used to excite the ion. The amplitude is varied to determine the regions where the ion is excited. For iterations $i = 1...6$, thresholds T_i ranging from 0.32 to 0.36 (dashed horizontal lines) are used to maximize the probability of success (Appendix A). Black dots indicate the average excitation probability observed when searching each of the two amplitude subspaces. Only $n = 5$ repetitions need be used for each scan due to the unambiguous, narrow feature inherent to the excitation sequences. With each iteration, searched locations where the ion was not found can be excluded (gray regions), the ion position is further localized, and subsequent pulse sequences search only in the remaining target area. (g) RMS error of the quantum-enhanced technique (filled circles) as a function of total coherent drive time clearly demonstrates the asymptotic $1/\tau$ scaling with total coherent drive time τ (solid curve). The dot-dashed curve is a fit showing scaling as $\tau^{-0.94\pm0.01}$, improving much more quickly than the classical $t^{-0.5}$ scaling (dashed curve).

$\Omega(x) \propto e^{-x^2/w^2}$ is monotonically decreasing; thus, an unambiguous mapping between position x and local Rabi frequency $\Omega(x)$ exists. (Relaxing this requirement would necessitate only one additional, short measurement to determine whether the ion was in the positive or negative half-space of the beam and would thus have negligible impact on the total imaging time.) A short sequence of length L_1 is initially applied to the ion. The initial search space is divided into a small number M of different locations identified by position $x_k, k = 1...M$; at each location x_k we perform n repetitions of the pulse sequence to attempt to drive the ion to $|e\rangle$. If the fraction of successful excitations of the ion out of n repetitions exceeds a user-specified threshold T at one of the M locations and at no others, the ion is considered to be found at that location. This localizes the ion to the position x_k to within an error $\Delta x_1 \propto 1/L_1$. The length of the sequence is then increased to L_2, and the resulting subspace of size Δx_1 is then itself divided into M search locations. This process is repeated, each iteration i localizing the ion to a corresponding $\Delta x_i \propto 1/L_i$ until the final Δx_f (achieved with sequence length L_f) is less than some specified uncertainty goal. We note that the total time for binary search scales as MnL_f and achieves positional error $\propto 1/L_f$, thus still retaining Heisenberg scaling.

Rather than physically moving our control beam, we instead vary its intensity and search for the amplitude Ω_{target} such that $\Omega_{target}e^{-x^2/w^2}t_0 = \pi$. We choose the ion position $x = w/\sqrt{2}$ to maximize the intensity gradient, and hence positional resolution, of our beam. The results are shown in Figure 5, plotting the achieved resolution versus total coherent illumination time. We use $M = 2$ searches per iteration of the sequence, $n = 5$ repetitions per search location, and proceed from the $L_1 = 3$ pulse sequence to the $L_6 = 99$ pulse sequence to localize the ion. The threshold T_i is optimized for each sequence (Supplemental Information). The entire binary search algorithm was repeated 100 times to accumulate statistics. A failure of the binary search algorithm, in which case the algorithm fails to identify the correct subspace in which the particle is located (see Supplemental Information for more details), occurred only once during the 100 trials, and only in the final iteration $i = 6$. After six iterations of this procedure, and taking into account the finite chance of failure, the ion is localized to within a rotation angle root-mean-square error (RMSE) $(\sigma_\theta)/(2\pi) = 0.004$. Given our beam waist of $140 \pm 10 \, \mu$m, the spatial resolution we achieve via binary search corresponds to positional RMS uncertainty $\sigma_x = 0.7 \pm 0.1 \, \mu$m, or an uncertainty of $(0.3 \pm 0.03)\%$ of the $1/e^2$ beam diameter of $280 \, \mu$m. Figure 5(g) shows the RMS error for the entire search taking into account the possibility of failure in a particular iteration, demonstrating resolution scaling with total coherent drive time τ as $\tau^{-0.94\pm0.01}$.

Comparison of quantum-enhanced imaging to classical imaging is not straightforward as the two techniques do not use the same laser beam (the coherent 674 nm beam

is used for quantum-enhanced imaging, while the 422 nm beam is used for classical imaging by scattering) and any comparison depends upon detailed experimental parameters. For our system, the quantum-enhanced technique exceeds the resolution achievable by classical scattering measurements, given the same total illumination time, for five or more iterations of the binary search (Supplemental Information). Residual slow beam positional fluctuations prevented further iterations of the binary search in this experiment. We note that, for these experiments, total experimental time is dominated by our relatively slow readout of ~ 1 ms per iteration, but much faster ion readouts (less than 150 μs) have been demonstrated [24]. This could possibly be implemented in our setup via adaptive measurement techniques or integrated detectors; we are currently pursuing efforts to demonstrate on-chip integrated detectors which could potentially enable much faster readout.

IV. DISCUSSION

In conclusion, we have demonstrated a new method of imaging which takes advantage of quantum coherence to achieve Heisenberg-limited scaling of the resolution. In our proof-of-principle experiment, we have achieved positional resolution to within 0.3% of the beam diameter and achieve spatial resolution of 0.7 μm, comparable to the probe laser wavelength of 674 nm. This is, to our knowledge, the first experiment to approach Heisenberg scaling of the resolution in an imaging task.

The technique has many possible uses in traditional imaging applications, especially for longer wavelengths (e.g., microwaves) where the size of the imaging beam may be large compared to details of interest. Furthermore, the selective excitation provided by these pulse sequences may be useful for site-selective control of trapped ions or other quantum systems, such as quantum dots or nitrogen vacancy centers. As one example, a long pulse sequence—with correspondingly high spatial selectivity—may be used to drive a target rotation in a particular qubit in an array while minimizing crosstalk effects on other nearby qubits. Our finite coherence time, limited by non-Markovian magnetic field drifts and laser phase noise, as well as residual beam jitter prevent us from achieving sub-wavelength resolution in this proof-of-principle experiment; however, modest improvements to the system would enable us to retain Heisenberg scaling out to many hundreds of pulses and achieve such resolution. Though Heisenberg scaling holds only within the system coherence time, after which classical scaling again takes over, the use of this technique can achieve a given resolution much faster than classical imaging methods.

Finally, while our proof-of-principle demonstration here images only one ion, the technique can straighforwardly be generalized to multiple targets within the search region, as long as the state detection allows determination of the total number of targets that have been excited—true for our trapped-ion detection here and for most other detection schemes based on fluorescence collection. In this case, each iteration of the search investigates any regions of the search space known to contain at least one target, with sub-regions not containing a target excluded from the later iterations (Supplemental Information).

V. ACKNOWLEDGEMENTS

[1] M. Hofmann, C. Eggeling, S. Jakobs, and S. W. Hell, Proceedings of the National Academy of Sciences of the United States of America **102**, 17565 (2005).

[2] M. J. Rust, M. Bates, and X. Zhuang, Nature Methods **3**, 793 (2006).

[3] E. Betzig, G. H. Patterson, R. Sougrat, O. W. Lindwasser, S. Olenych, J. S. Bonifacino, M. W. Davidson, J. Lippincott-Schwartz, and H. F. Hess, Science **313**, 1642 (2006).

[4] A. S. Trifonov, J.-C. Jaskula, C. Teulon, D. R. Glenn, N. Bar-Gill, and R. L. Walsworth, in *Advances in Atomic, Molecular, and Optical Physics*, Advances In Atomic, Molecular, and Optical Physics, Vol. 62, edited by P. R. B. Ennio Arimondo and C. C. Lin (Academic Press, 2013) pp. 279 – 302.

[5] E. Betzig and J. K. Trautman, Science **257**, 189 (1992).

[6] S. W. Hell, Science **316**, 1153 (2007).

[7] V. Giovannetti, S. Lloyd, and L. Maccone, Science **306**, 1330 (2004).

[8] R. Demkowicz-Dobrzanski, J. Kolodynski, and M. Guta, Nature Communications **3**, 1063 (2012).

[9] N. F. Ramsey, Phys. Rev. **78**, 695 (1950).

[10] N. V. Vitanov, Phys. Rev. A **84**, 065404 (2011).

[11] J. A. Jones, Phys. Rev. A **87**, 052317 (2013).

[12] G. H. Low, T. J. Yoder, and I. L. Chuang, Phys. Rev. A **89**, 022341 (2014).

[13] G. H. Low, T. J. Yoder, and I. L. Chuang, Phys. Rev. Lett. **114**, 100801 (2015).

[14] G. Waldherr, J. Beck, P. Neumann, R. S. Said, M. Nitsche, M. L. Markham, D. J. Twitchen, J. Twamley, F. Jelezko, and J. Wrachtrup, Nature Nanotechnology **7**, 105 (2012).

[15] G. Puentes, G. Waldherr, P. Neumann, G. Balasubramanian, and J. Wrachtrup, Scientific Reports **4**, 4677 (2014).

[16] J. Sastrawan, C. Jones, I. Akhalwaya, H. Uys, and M. J. Biercuk, arXiv:1407.3902v2 [quant-ph] (2016).

[17] K. Arai, C. Belthangady, H. Zhang, N. Bar-Gill, S. De-Vience, P. Cappellaro, A. Yacoby, and R. Walsworth, Nature Nanotechnology **10**, 859 (2015).

[18] D. J. Wineland, C. Monroe, W. M. Itano, D. Leibfried, B. E. King, and D. M. Meekhof, J. Res. Natl. Inst. Stand. Technol. **103**, 259 (1998).

[19] C. Shen, Z.-X. Gong, and L.-M. Duan, Phys. Rev. A **88**, 052325 (2013).

[20] J. T. Merrill, S. C. Doret, G. Vittorini, J. P. Addison, and K. R. Brown, Phys. Rev. A **90**, 040301 (2014).

[21] G. H. Low, T. J. Yoder, and I. L. Chuang, arXiv:1603.03996v1 [quant-ph] (2016).

[22] J. M. Sage, A. J. Kerman, and J. Chiaverini, Phys. Rev. A **86**, 013417 (2012).

[23] N. Akerman, N. Navon, S. Kotler, Y. Glickman, and R. Ozeri, New Journal of Physics **17**, 113060.

[24] A. H. Myerson, D. J. Szwer, S. C. Webster, D. T. C. Allcock, M. J. Curtis, G. Imreh, J. A. Sherman, D. N. Stacey, A. M. Steane, and D. M. Lucas, Phys. Rev. Lett. **100**, 200502 (2008).